In-Depth Understanding of the Morphology Effect of α-Fe_2O_3 on Catalytic Ethane Destruction

Yanfei Jian,[†,○] Tingting Yu,[‡,○] Zeyu Jiang,[†] Yanke Yu,[†,§] Mark Douthwaite,[∥] Jingyin Liu,[⊥] Reem Albilali,[#] and Chi He*[,†,∥,▽]

[†]State Key Laboratory of Multiphase Flow in Power Engineering, School of Energy and Power Engineering, Xi'an Jiaotong University, Xi'an 710049, Shaanxi, P.R. China

[‡]State Key Laboratory of Heavy Oil Processing, China University of Petroleum, Beijing 102249, P.R. China

[§]Department of Chemical Engineering, Columbia University, New York, New York 10027, United States

[∥]Cardiff Catalysis Institute, School of Chemistry, Cardiff University, Main Building, Park Place, Cardiff CF10 3AT, U.K. [⊥]Yunhui Co., Ltd., Shanghai 201199, P.R. China

[#]Department of Chemistry, College of Science, Imam Abdulrahman Bin Faisal University, P.O. Box 1982, Dammam 31441, Saudi Arabia

[▽]National Engineering Laboratory for VOCs Pollution Control Material & Technology, University of Chinese Academy of Sciences, Beijing 101408, P.R. China

* Supporting Information

ABSTRACT: Shape effects of nanocrystal catalysts in different reactions have attracted remarkable attention. In the present work, three types of α-Fe_2O_3 oxides with different micromorphologies were rationally synthesized via a facile solvothermal method and adopted in deep oxidation of ethane. The physicochemical properties of prepared materials were characterized by XRD, N_2 sorption, FE-SEM, HR-TEM, FTIR, in situ DRIFTS, XPS, Mössbauer spectroscopy, in situ Raman, electron energy loss spectroscopy, and H_2-TPR. Moreover, the formation energy of oxygen vacancy and surface electronic structure on various crystal faces of α-Fe_2O_3 were explored by DFT calculations. It is shown that nanosphere-like α-Fe_2O_3 exhibits much higher ethane destruction activity and reaction stability than nanocube-like α-Fe_2O_3 and nanorod-like α-Fe_2O_3 due to larger amounts of oxygen vacancies and lattice defects, which greatly enhance the concentration of reactive oxygen species, oxygen transfer speed, and material redox property. In addition to this, DFT results reveal that nanosphere-like α-Fe_2O_3 has the lowest formation energy of oxygen vacancy on the (110) facet (E_{vo} (110) = 1.97 eV) and the strongest adsorption energy for ethane (−0.26 eV) and O_2 (−1.58 eV), which can accelerate the ethane oxidation process. This study has deepened the understanding of the face-dependent activities of α-Fe_2O_3 in alkane destruction.

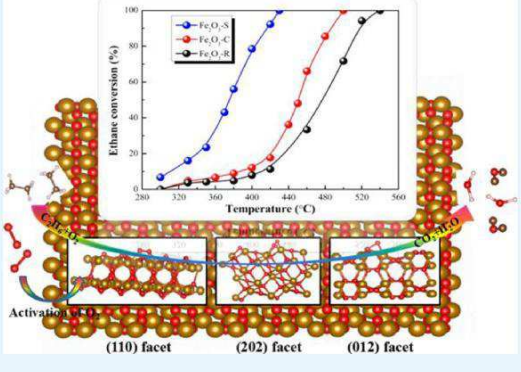

KEYWORDS: Fe_2O_3, oxygen vacancy, ethane, catalytic oxidation, DFT calculation

1. INTRODUCTION

The emission of volatile organic compounds (VOCs) during industrial processes leads to great environment hazards such as ozone depletion and photochemical smog.[1] Furthermore, many VOCs are carcinogenic and toxic. It is difficult to destroy linear short-chain alkanes. Ethane is an inert alkane that vastly existed in natural gas (1.8−5 mol %) and currently mainly used as a fuel for industrial refining processes.[2] Catalytic combustion can be considered as one of the most effective approaches for the low-energy elimination of VOCs.[3] The Pt- and Pd-based materials are the most efficient catalysts for total oxidation of hydrocarbons currently, but the use of noble metal-free metal oxides offers considerable economic advantages.[4] Among them, CoO_x, MnO_x, and FeO_x materials constitute another choice to Pt/Pd-based catalysts. However, common CoO_x, MnO_x, and FeO_x oxides are less active than the supported noble metal catalysts in most cases. Comparatively, the environment-friendly FeO_x oxides possess much higher anti-sintering ability than the CoO_x and MnO_x materials, which suffer from catalytic deactivation at elevated temperatures, endowing FeO_x oxides a kind of promising catalysts for inert alkane destruction, although the low-temperature activity of FeO_x is more or less lower than that of CoO_x and MnO_x catalysts.[5−7] Hematite (α-Fe_2O_3), based

on hexagonal close packing of oxygen with iron in two-thirds of the octahedral vacancies, is generally adopted as an heterogeneous catalyst due to its high resistance, low cost to deactivation, and environment-friendly properties.[9]

Controlling the morphology of the nanoparticles can influence their catalytic performance because the different topographies of the particles can expose different crystal faces.[10] It is known that facet engineering causes different chemical and physical properties in nanomaterials due to distortion of the electronic structures and various exposed atoms in crystal surfaces having different exposed faces. Many applications, for example, gas sensing, energy conversion and storage, and heterogeneous catalysis are very alive to surface structures. As such, the promise of high energy and reactivity in engineering surface structures and exposure-specific aspects is becoming a promising research direction.[11] Different kinds of nanomaterials with special forms and structures, for example, nanowires,[12] nanorods,[13] nanotubes,[14] nanobelts,[15] nano-plates,[16] and nanorings,[17] have been synthesized by various methods. Li et al.[18] compared the catalytic property of CeO_2 nanoparticles and CeO_2 nanorods in CO oxidation and found that the catalytic activity of CeO_2 nanorods is greater than nanoparticles because the exposed {110} and {100} planes have higher oxygen storage capacity. Similarly, Xie et al.[19] proposed that CeO_2 nanorods that exposed the {110} and {001} facets show a better CO conversion efficiency than CeO_2 with {111} facets. Qiu et al.[20] proposed that the propane adsorption energies on different crystal facets of MnO_2 are different ($\alpha(310) > \gamma(120) > \beta(110) > \delta(001)$), which influence its propane oxidation activity. Using different methods such as thermal decomposition and hydrothermal methods synthesize α-Fe_2O_3 with different crystals.[21] Kouotou et al.[1] found that the α-Fe_2O_3 thin film exhibits good performance toward catalytic combustion of C_3H_6. Zheng et al.[8] found that the α-Fe_2O_3 nanoparticles that has a uniform quasi-cubic structure with six identical {110} planes exhibit outstanding catalytic performance for CO oxidation because the exposed {110} planes have a high density of Fe atoms.

In this work, three kinds of α-Fe_2O_3 with different micromorphologies and exposed facets (i.e., nanosphere-like α-Fe_2O_3 (Fe_2O_3-S), nanocube-like α-Fe_2O_3 (Fe_2O_3-C), and nanorod-like α-Fe_2O_3 (Fe_2O_3-R), respectively, with predom-inantly exposed (110), (202), and (012) facets) were rationally synthesized, and the synthesized catalysts were extensively characterized by different technologies including electron energy loss spectroscopy (EELS), X-ray diffraction (XRD), Fourier transform infrared spectroscopy (FTIR), high-reso-lution transmission electron microscopy (HR-TEM), Mössba-uer spectroscopy, field-emission scanning electron microscopy (FE-SEM), X-ray photoelectron spectroscopy (XPS), Raman/ in situ Raman, and temperature-programmed reduction by hydrogen (H_2-TPR). In addition, the formation energy of oxygen vacancy and surface electronic structure on different crystal faces of α-Fe_2O_3 were studied by the density functional theory (DFT) calculations. The catalytic performance of obtained materials toward the total oxidation of ethane was studied, and the effect of oxygen vacancy, lattice defect, and crystal facets on catalyst surface chemical composition, reduction property, and catalytic performance was discussed in detail.

2. EXPERIMENTAL SECTION

The detailed experimental section is described in Text S1 (Supporting Information).

3. RESULTS

3.1. Structural Property. As shown in Figure 1, the micromorphologies of Fe_2O_3-S, Fe_2O_3-C, and Fe_2O_3-R

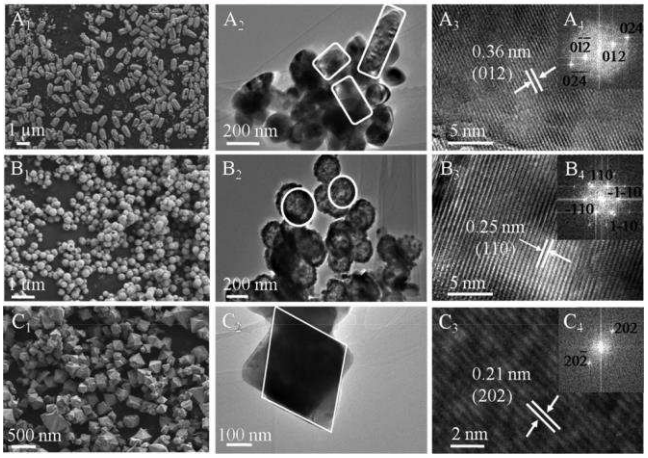

Figure 1. FE-SEM and HR-TEM images of (A, A_1, A_2) Fe_2O_3-R, (B, B_1, B_2) Fe_2O_3-S, and (C, C_1, C_2) Fe_2O_3-C (insets: FFT images of (A_3) Fe_2O_3-R, (B_3) Fe_2O_3-S, and (C_3) Fe_2O_3-C).

catalysts were determined by FE-SEM and HR-TEM. Fe_2O_3-R has a uniform diameter of 100−200 nm with a length in the range of 100−1000 nm (Figure 1A_1,A_2). A lattice spacing of 0.36 nm attributed to the (012) plane can be observed (Figure 1A_3), and similar results can be obtained from the fast Fourier transformation (FFT) of Fe_2O_3-R (Figure 1A_4). The Fe_2O_3-S sample shows a spherical morphology with a rough surface, and the average diameter of particles is 200 ± 20 nm (Figure 1B_1,B_2). Results of HR-TEM (Figure 1B_3) and FFT transformation (Figure 1B_4) confirm that Fe_2O_3-S is enclosed by the (110) planes mainly with a lattice spacing of 0.25 nm. Figure 1C_1,C_2 suggests that Fe_2O_3-C has an octahedron shape with a side size of 240 ± 10 nm. HR-TEM image (Figure 1C_3) and corresponding FFT (Figure 1C_4) reveal that the lattice fringe is 0.21 nm, implying that Fe_2O_3-C is mainly enclosed by (202) facets.

XRD patterns of prepared materials are shown in Figure 2. The diffraction peaks of Fe_2O_3-S, Fe_2O_3-C, and Fe_2O_3-R samples agree well with the α-hematite crystallographic phase of Fe_2O_3 (rhombohedral structure, JCPDS 33-0664, space group R-3c) with lattice constants of a = 0.5035 nm and c = 1.3740 nm. The lattice constants of prepared materials (Fe_2O_3-S: a = 0.5039 nm, c = 1.3746 nm; Fe_2O_3-C: a = 0.5034 nm, c = 1.3750 nm; Fe_2O_3-R: a = 0.5038 nm, c = 1.3748 nm) were calculated by the least-square fitting method, which are in accordance with the above data. The peak width at half height of Fe_2O_3-S diffractions is wider than those of Fe_2O_3-C and Fe_2O_3-R, indicating that Fe_2O_3-S has a smaller grain size than Fe_2O_3-C and Fe_2O_3-R materials, in agreement with the data calculated by the Scherrer equation (average grain sizes of Fe_2O_3-S, Fe_2O_3-C, and Fe_2O_3-R are 20, 177, and 189 nm, respectively).

The specific surface area and porosity of Fe_2O_3-S, Fe_2O_3-C, and Fe_2O_3-R materials were studied by low-temperature N_2 sorption, as displayed in Figure S1 and Table 1. It can be

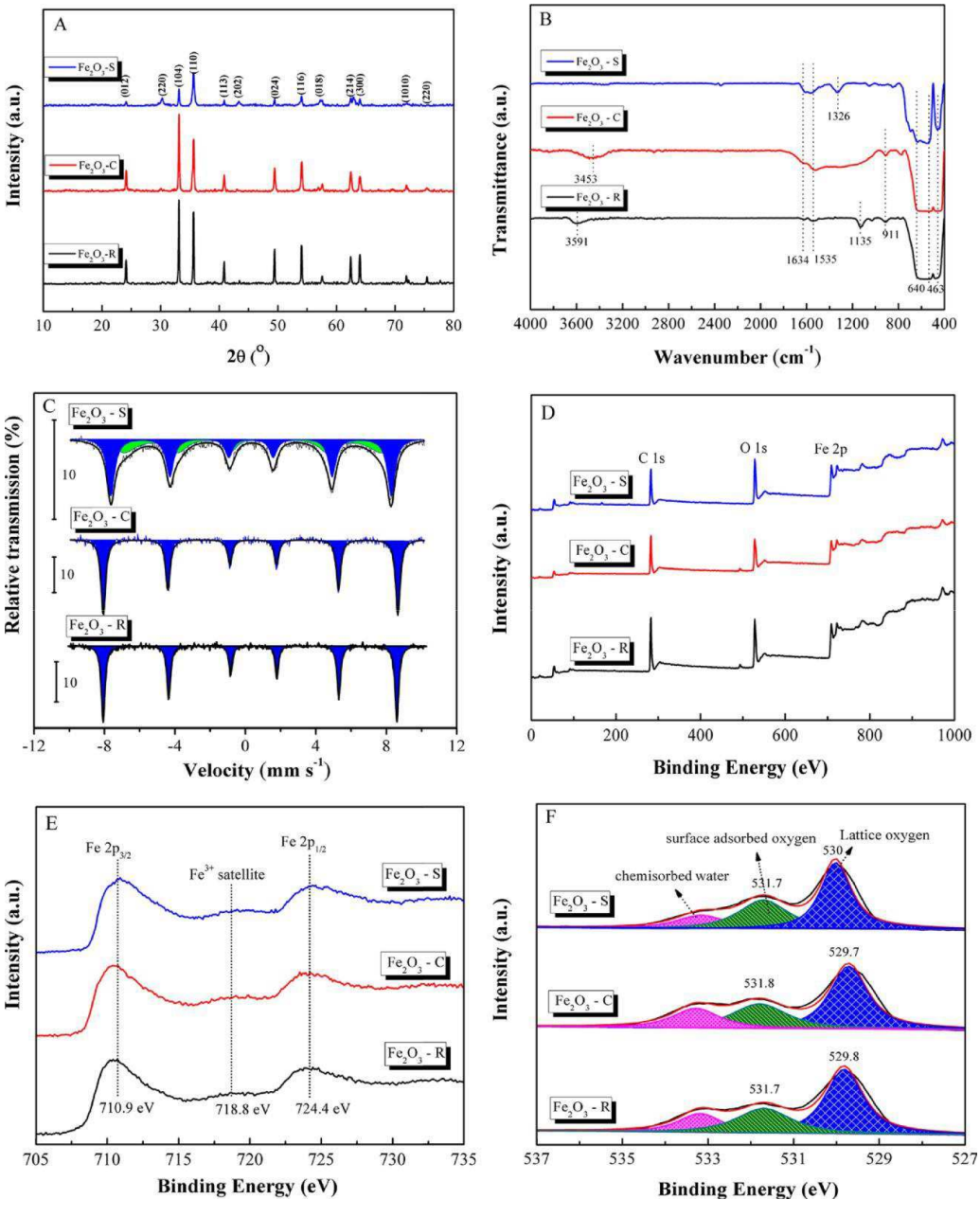

Figure 2. (A) XRD patterns, (B) FT-IR spectra, (C) room-temperature Mössbauer spectra, and (D) XPS survey spectra and corresponding (E) Fe 2p and (F) O 1s XPS spectra of prepared catalysts.

Table 1. Textural Property of Prepared Materials

sample	S_{BET}[a] ($m^2\ g^{-1}$)	V_t[b] ($cm^3\ g^{-1}$)	C_s[c] (nm)	D_p[d] (nm)	I_{H1}[e] ($\times10^{-4}$ mmol $g^{-1}\ s^{-1}$)	I_{H2}[e] ($\times10^{-4}$ mmol $g^{-1}\ s^{-1}$)
Fe_2O_3-S	44.5	0.11	20	7.5	1.41	1.51
Fe_2O_3-C	8.5	0.02	177	3.5	0.21	0.23
Fe_2O_3-R	8.8	0.04	189	4.7	0.14	0.18

[a]Specific surface area obtained at $P/P_0 = 0.05-0.30$. [b]Total pore volume estimated at $P/P_0 = 0.99$. [c]Crystal size obtained from the results of XRD. [d]BJH pore diameter calculated from the desorption branch. [e]Initial H_2 consumption rates of synthesized catalysts at 340 and 350 °C.

observed in Table 1 that the specific surface area, total pore volume, and average pore diameter of Fe_2O_3-S (44.5 $m^2\ g^{-1}$, 0.11 $cm^3\ g^{-1}$, and 7.5 nm, respectively) are much higher than those of Fe_2O_3-C (8.5 $m^2\ g^{-1}$, 0.02 $cm^3\ g^{-1}$, and 3.5 nm, respectively) and Fe_2O_3-R (8.8 $m^2\ g^{-1}$, 0.04 $cm^3\ g^{-1}$, and 4.7 nm, respectively). Figure S1A suggests that the Fe_2O_3-S sample possesses a type IV isotherm with a clear H3-type hysteresis loop, characteristic of a mesoporous material.[22] The pore size distribution (PSD) was obtained by the Barrett−Joyner−Halenda (BJH) method (Figure S1, inset). Fe_2O_3-S shows unimodal pore size distribution with a predominant pore radius of around 20 nm, indicating the homogeneous distribution of pores;[22] however, Fe_2O_3-C and Fe_2O_3-R with type III isotherms can be observed (Figure S1B,C),[23] and the

pore size distribution curves of Fe_2O_3-C and Fe_2O_3-R show several mesopore peaks in the range of 15−45 nm, indicating the heterogeneity distribution of pores, which is considered to be mainly caused by an interspace between the component nanoparticles.[22]

3.2. Surface Property. Figure 2B shows the FTIR spectra of Fe_2O_3-S, Fe_2O_3-C, and Fe_2O_3-R materials. All samples show a broad band at 463−640 cm^{-1}. This band can be attributed to the Fe−O bond vibration of Fe_2O_3.[24] The bands at 1634 and 1535 cm^{-1} are assigned to the bending and vibration of H_2O molecules and C−O bond, respectively.[25] The strong absorption peaks at 3453 cm^{-1} (over Fe_2O_3-C) and 3591 cm^{-1} (over Fe_2O_3-R) can be assigned to the O−H stretching vibration of intermolecular hydrogen bonding,[25] and the weak band at 911 cm^{-1} over Fe_2O_3-C and Fe_2O_3-R can be attributed to the vibration of Fe-OH.[26] For Fe_2O_3-R, the peak at 1135 cm^{-1} can be assigned to the asymmetric and symmetric stretching vibrations of sulfonic acid group ($-SO_3^-$).[27] The band at around 1326 cm^{-1} over Fe_2O_3-S corresponds to the typical stretching mode of C−N heterocycles.[28]

Figure 2C shows the room-temperature transmission Mössbauer spectra of Fe_2O_3-S, Fe_2O_3-C, and Fe_2O_3-R materials. The fitted hyperfine parameters of subspectra, for example, isomer shifts (IS), quadruple splittings (QS), magnetic hyperfine field (Bhf), and resonance half-height line widths (LW), are listed in Table 2. The Mössbauer spectrum of Fe_2O_3-S is well fitted with two sextets, and the spectra of Fe_2O_3-C and Fe_2O_3-R materials are well fitted with one sextet. The IS values of all samples listed in Table 2 are lower than 0.5 mm s^{-1}, indicating that the valence state of iron in all catalysts is +3.[29] The sextets with Bhf around 51 T can be assigned to the characteristic of high-spin Fe^{3+} ions in octahedral coordination of the α-Fe_2O_3 phase (hematite).[30] The room-temperature existence of a doublet in the Mössbauer spectrum is related to the presence of superparamagnetic nanoparticles, which have critically lower dimension based on the results of XRD (Figure 2A).[31] The first sextet component with an IS value of 0.32 mm s^{-1} (about 57.3%) is assigned to the presence of large hematite particles, whereas the second sextet component with an IS value of 0.41 mm s^{-1} (about 42.7%) is ascribed to small particles.[32] In Mössbauer spectroscopy, because of the magnetic field distribution caused by local lattice distortion, the line width Γ of some spectral components is widened, and the presence of vacancies in the nearest neighbor of the Mossbauer probe or a sufficiently large impurity atom can also be observed.[32] Table 2 shows that the line widths Γ of Fe_2O_3-S, Fe_2O_3-C, and Fe_2O_3-R are 0.55, 0.31, and 0.25 mm s^{-1}, respectively, suggesting that the amount of lattice defects in prepared materials are following the order of Fe_2O_3-S > Fe_2O_3-C > Fe_2O_3-R.

Table 2. Characterized Results of Synthesized Materials Obtained from the Mössbauer Spectra

sample	IS[a] (mm s^{-1})	QS[b] (mm s^{-1})	LW[c] (mm s^{-1})	Bhf[d] (T)	abundance (%)
Fe_2O_3-S	0.32	0.002	0.55	49.5	57.3
	0.41	0	0.49		42.7
Fe_2O_3-C	0.37	−0.15	0.31	51.9	100
Fe_2O_3-R	0.37	−0.21	0.25	51.8	100

[a]Isomer shift (relative to the source). [b]Quadrupole shift/splitting.

The surface chemical composition and chemical states of prepared materials were investigated by XPS, as displayed in Figure 2D−F and Table 3. The doublet peaks of Fe $2p_{1/2}$ and Fe $2p_{3/2}$ are located at around 724.4 and 710.8 eV, respectively (Figure 2E), in well agreement with typical binding energies of Fe^{3+} in Fe_2O_3.[33,34] Besides, a satellite peak at around 718.8 eV is also attributed to the characteristic peak of Fe_2O_3.[33,34] The binding energy between the satellite and Fe $2p_{3/2}$ peaks is 7.90 eV for all samples, which suggests the presence of α-Fe_2O_3,[34] consistent with the results of Mössbauer spectra (Figure 2C). In catalytic oxidation reactions, relative ratios and status of different oxygen species play crucial roles, and O 1s XPS spectra are shown in Figure 2F. The O 1s spectra of all materials can be divided into three peaks. The peaks located at 529.4−530.6, 530.8−532.0, and 532.1−532.2 eV can be assigned to the lattice oxygen for metal oxides (O_α), adsorbed oxygen (O_β), and surface oxygen by adsorbed water species (O_λ), respectively.[35,36] Generally, because of the excellent fluidity of O_β, the high relative concentration of O_β on the surface of the catalyst can be correlated with the high activity in the oxidation reaction. It is shown in Table 3 that the ratios of O_β/O_α are approximately 0.72, 0.59, and 0.55 for Fe_2O_3-S, Fe_2O_3-C, and Fe_2O_3-R, respectively, suggesting that the largest amount of O_β species existed over the Fe_2O_3-S material. In addition to this, the O_α peak of Fe_2O_3-S (530 eV) shifts toward higher binding energy than those of Fe_2O_3-C (529.7 eV) and Fe_2O_3-R (529.8 eV), indicating that there are more defective oxygen sites over Fe_2O_3-S than the other materials.[37]

We further divided and analyzed the Fe $2p_{3/2}$ XPS peak (Figure 2E) to get some understanding of sample character-istics, as shown in Figure 3. Four multiplet peaks (except the surface peak and pre-peak) in a bind energy range of 708−716 eV can be obtained.[37,38] It is found that peak 1 is more intense (Figure 3D) and its peak area is larger than the second multiplet peak (peak 2) for samples. For hematite particles, the higher integral peak area and intensity of the first multiple peak (peak 1) are expected.[37,38] The splitting indicates that some Fe^{3+} cations in hematite samples have tetrahedral coordination, and all cations in this phase should have octahedral coordination.[37,38] It can be seen in the ratios of area between peak 1 and peak 2 (Table S1) in different catalysts; that is, the

Table 3. XPS Results of Prepared Catalysts

	binding energy (eV)				
sample	Fe^{3+} $2p_{1/2}$	Fe^{3+} $2p_{3/2}$	O_α[a]	O_β[b]	O_β/O_α[c]
Fe_2O_3-S	724.4	710.9	530 (39555.3)	531.7 (28550.2)	0.72
Fe_2O_3-C	724.4	710.8	529.7 (30264.4)	531.8 (17815.3)	0.59
Fe_2O_3-R	724.4	710.8	529.8 (48470.8)	531.7 (27038.9)	0.55

[a]Lattice over prepared catalysts (corresponding peak areas are listed in brackets). [b]Adsorbed oxygen over prepared catalysts (corresponding peak areas are listed in brackets). [c]Peak area ratio.

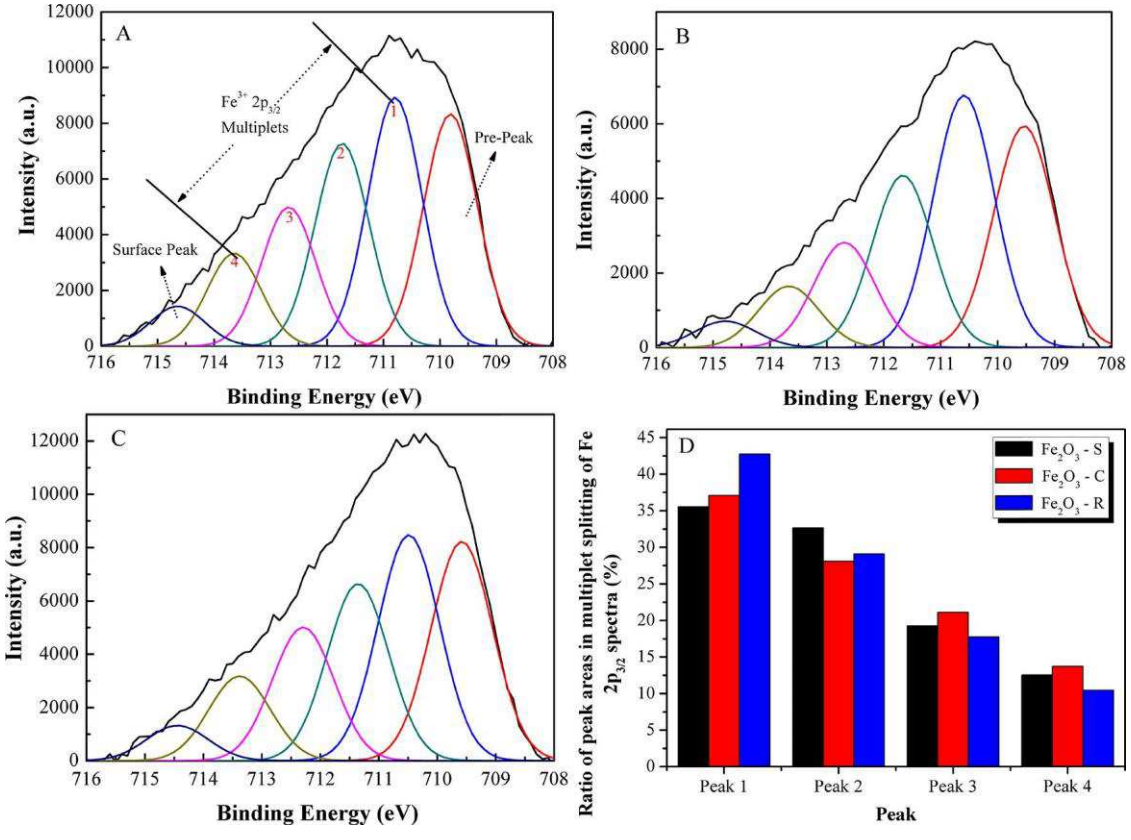

Figure 3. Analysis of the multiplet splitting of the Fe $2p_{3/2}$ peak of each hematite nanomaterial from the XPS results of (A) Fe_2O_3-S, (B) Fe_2O_3-C, and (C) Fe_2O_3-R. (D) Corresponding ratio of peak areas in multiplet splitting of Fe $2p_{3/2}$ for Fe_2O_3-S, Fe_2O_3-C, and Fe_2O_3-R.

ratio closer to 1 indicates that some of the Fe^{3+} cations are tetrahedrally coordinated in the catalyst. It is similar to γ-Fe_2O_3 where some of the Fe^{3+} cations are tetrahedrally coordinated.[37] It can been explained that, with nanoparticles becoming smaller, dimension-dependent structural conversion may occur, resulting in surface hematite defects and leading to the appearance of tetrahedrally coordinated Fe^{3+} cations.[39] As such, the Fe_2O_3-S sample with the smallest grain size (20 nm, close to the maximum diameter of defect frequency (30 nm)) possesses more defects on the surface than Fe_2O_3-C (177 nm) and Fe_2O_3-R (189 nm).

To have more details about the phase of the synthesized materials, Raman spectroscopy was utilized as shown in Figure 4. The bands at 219 and 499 cm^{-1} are attributed to the A_{1g} mode of α-Fe_2O_3, and those observed at 286, 405, and 608 cm^{-1} correspond to the E_g mode of α-Fe_2O_3.[1] The interactions between two magnons formed on antiparallel spins, typically of α-Fe_2O_3 (Figure 4A),[40] can lead to the appearance of the broad band between 1200 and 1400 cm^{-1}. By comparing those of Fe_2O_3-C and Fe_2O_3-R, the peaks over the Raman spectrum of Fe_2O_3-S are broader and weaker, demonstrating that the hematite nanoparticles with smaller crystalline size and long-range disordered accumulation in the structure can result in many factors such as poor crystallization, lattice defects, and oxygen vacancies.[41] The Raman spectra region between 550 and 750 cm^{-1} was extracted and further divided into three peaks (E_g of 608 cm^{-1}, LO of 660 cm^{-1}, and T of 690 cm^{-1}), as shown in Figure 4B−D. The intensity of LO and T peaks can explain that the degree of disorder in the lattice of hematite and the existence of lattice defects on the surface of nanoparticles are related, respectively.[37] As shown in Table S2, the intensity of the LO band decreases in the order of Fe_2O_3-S (15.77) > Fe_2O_3-C (6.68) > Fe_2O_3-R (3.59), similar with that the T band (Fe_2O_3-S (11.42) > Fe_2O_3-C (6.55) > Fe_2O_3-R (4.70)). Above results suggest that Fe_2O_3-S has the largest amounts of structural defects than Fe_2O_3-C and Fe_2O_3-R materials, in agreement with the result of Mössbauer spectroscopy (Figure 2C).

Figure 5 shows the in situ Raman spectra of prepared Fe_2O_3 samples. It is found that the intensity of all Raman peaks decrease dramatically (becoming wider) with the increase in temperature. For hematite, the expansion of these bands is a size-dependent phenomenon caused by uneven strain broadening associated with particle size dispersion and phononic construction.[42] Especially, the band at about 608 cm^{-1} becomes broader and weaker for all materials due to the increase in oxygen vacancies.[43] Figure S2 displays the related contour map of the in situ Raman spectra of prepared materials. It can be observed that the Raman peaks of Fe_2O_3-S reduce to the minimum at only 100 °C, whereas the related temperatures for Fe_2O_3-C and Fe_2O_3-R materials are 250 and 350 °C, respectively, implying that Fe_2O_3-S is more likely to form oxygen vacancies than Fe_2O_3-C and Fe_2O_3-R. The data are collected by EELS, and a zero loss peak value on energy scale calibration was performed with a low-loss-area deconvolution to minimize the multiple scattering effect.[44] Figure 6A represents the EELS spectra of oxygen K-edge energy-loss near-edge fine structure (ELNES) for Fe_2O_3-S, Fe_2O_3-C, and Fe_2O_3-R. Four peaks, denoted as a, b, c, and d, can be found in all materials.[44] In general, a derives from the O 1s to 2p core level hybridized with the Fe 3d orbital, and b originates from the O 2p states hybridized with the transition

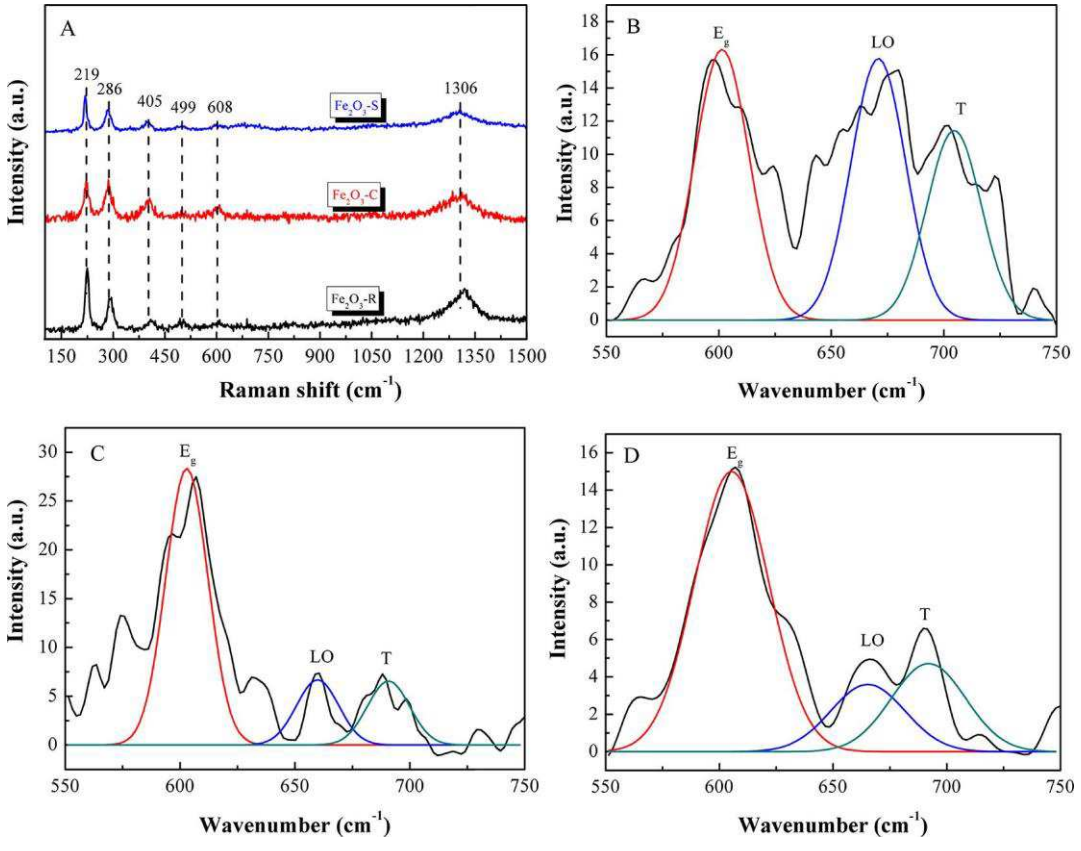

Figure 4. (A) Full Raman spectra of all hematite nanomaterials and corresponding peak deconvolution of the Eg, LO, and T bands of (B) Fe_2O_3-S, (C) Fe_2O_3-C, and (D) Fe_2O_3-R samples.

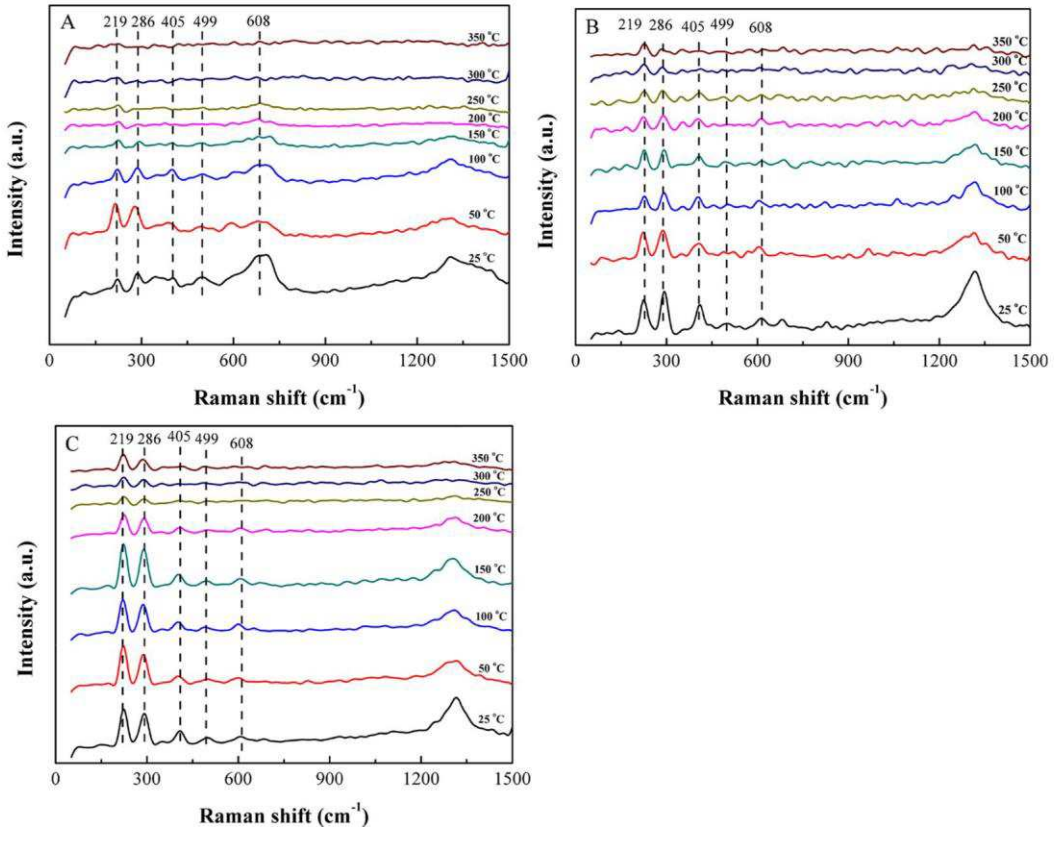

Figure 5. In situ Raman spectra of (A) Fe_2O_3-S, (B) Fe_2O_3-C, and (C) Fe_2O_3-R.

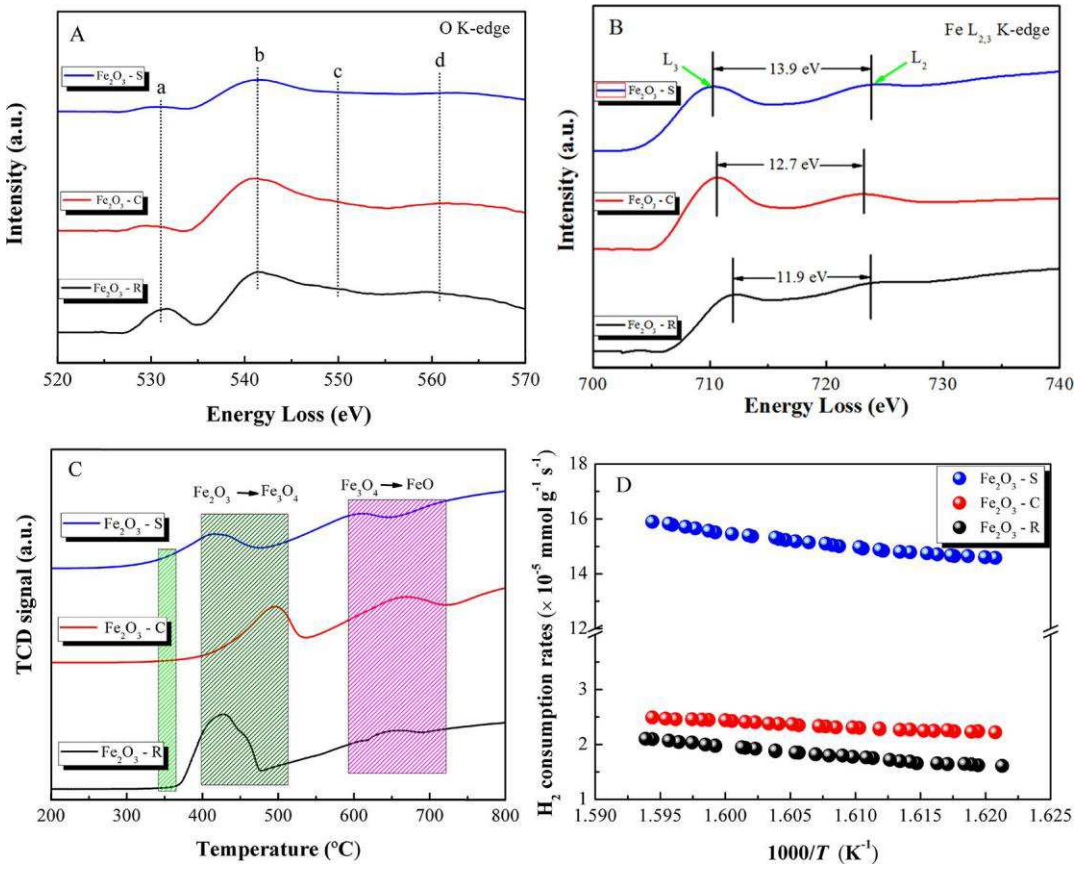

Figure 6. EELS spectra of (A) oxygen K-edge ELNES and (B) Fe L-edge of α-Fe_2O_3. (C) H_2-TPR profiles and (D) initial H_2 consumption rates of synthesized catalysts.

metal 4s and 4p states. The c and d result from the scattering of the third and first oxygen coordination shells by outgoing or backscattering electrons.[44,45] It is obvious that the intensities of a and b of Fe_2O_3-S are lower than those of Fe_2O_3-C and Fe_2O_3-R samples (Fe_2O_3-S < Fe_2O_3-C < Fe_2O_3-R). The intensity decreases of a and b are caused by the oxygen vacancies inside the prepared materials, resulting in diminish-ing hybridization of metal 3d and O 2p orbits.[44] As such, it can be demonstrated that the amount of oxygen vacancies in all materials follows the order of Fe_2O_3-S > Fe_2O_3-C > Fe_2O_3-R. The ionization state of the metal cation can be provided by the L edge via the determination of intensity and relative position of individual L_3 and L_2 edges, respectively.[44] Figure 6B represents the Fe $L_{2,3}$ K-edge spectra of Fe_2O_3-S, Fe_2O_3-C, and Fe_2O_3-R. It can be noted that the L_3 line is the transition $2p_{3/2} \rightarrow 3d_{3/2}3d_{5/2}$, whereas the L_2 line refers to the transition $2p_{1/2} \rightarrow 3d_{3/2}$. For Fe_2O_3-S, the L_3 line is located at 710.3 eV and is separated by 13.9 eV from the L_2 line; however, the corresponding data are 710.5 and 12.7 eV and 711.9 and 11.9 eV for Fe_2O_3-C and Fe_2O_3-R, respectively. The chemical shift of L_3 lines likely results from oxygen vacancies, which partially decrease the oxidation states of Fe cations from Fe^{3+} to Fe^{2+}.[44,45] By comparing the degree of chemical shift of L_3 lines, it can be concluded that Fe_2O_3-S has the maximum amount of oxygen vacancies, followed by Fe_2O_3-C and Fe_2O_3-R, in accordance with the result of oxygen K-edge energy loss (Figure 6A).

3.3. Reducibility. Figure 6C and Figure S3 represent the H_2-TPR profiles of prepared materials, and all samples present two H_2 consumption stages due to the reduction of Fe_2O_3 to Fe_3O_4 and Fe_3O_4 to FeO.[36,46] The theoretical H_2 consumption amount for the reduction of Fe_2O_3 to Fe_3O_4 is 2.09 mmol g^{-1}. In the present work, the H_2 consumption amount of the first reduction stage for Fe_2O_3-S, Fe_2O_3-C, and Fe_2O_3-R samples are 2.07, 2.06 and 2.03 mmol g^{-1}, respectively, indicating that a substantial fraction of Fe^{3+} in α-Fe_2O_3 can be reduced to Fe^{2+} below 550 °C. For the purpose of comparing the reducibility at low temperature for the prepared samples, the initial H_2 consumption of the first reduction band was calculated for each sample before phase transition (the initial H_2 consumption of the first reduction band of the catalyst is less than 25%),[49] and the results are shown in Figure 6D. It can be noted that the initial H_2 consumption rate (I_{H2}, Table 1) of Fe_2O_3-S is much higher than those of Fe_2O_3-C and Fe_2O_3-R with an order of Fe_2O_3-S ≫ Fe_2O_3-C > Fe_2O_3-S. For instance, the I_{H2} of Fe_2O_3-S at 350 °C is 1.5×10^{-4} mmol g^{-1} s^{-1}, over six times higher than those of Fe_2O_3-C and Fe_2O_3-R. To investigate the nature of oxygen species involved in ethane oxidation, O_2-TPD experiments were conducted. As shown in Figure S4, all samples display two desorption peaks centered at around 150 and 500 °C. The first peak (α_1-oxygen) can be attributed to the physically adsorbed oxygen or O_2^- (ad) species.[48] The second peak (α_2-oxygen) is associated with the desorption of chemically adsorbed oxygen O^- species. Generally speaking, O^- often belongs to the surface active oxygen,[47] and these surface reactive oxygen species are known to promote the catalytic oxidation activity.[47] Compared with the Fe_2O_3-S sample, the O_2 desorption peaks of Fe_2O_3-C and Fe_2O_3-R materials obviously shift to higher temperatures, and the intensity of these peaks is also much weaker as a result of

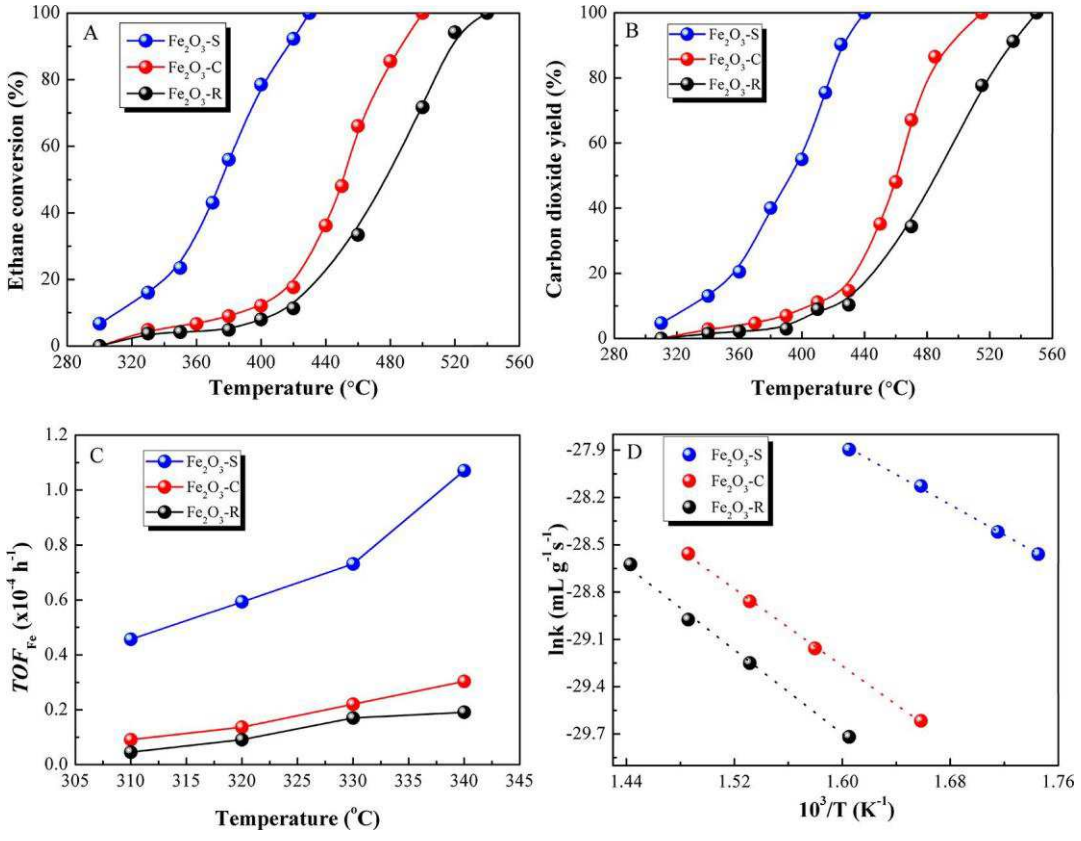

Figure 7. (A) Ignition curve, (B) CO_2 yield, (C) TOF, and (D) apparent activation energy (E_a) of different catalysts for ethane oxidation.

Table 4. Catalytic Performance of Prepared Materials for Ethane Oxidation

sample	T_{50}[a] (°C)	T_{90}[a] (°C)	r_1[b] ($\times10^{-3}$ mmol mL^{-1} h^{-1})	r_2[b] ($\times10^{-3}$ mmol mL^{-1} h^{-1})	TOF_{Fe1}[c] ($\times10^{-4}$ h^{-1})	TOF_{Fe2}[c] ($\times10^{-4}$ h^{-1})	E_a[d] (kJ mol^{-1})
Fe_2O_3-S	380	415	0.46	0.67	0.73	1.07	39.7
Fe_2O_3-C	450	485	0.14	0.19	0.22	0.30	50.9
Fe_2O_3-R	480	515	0.11	0.12	0.17	0.19	55.3

[a]Temperatures at 50 and 90% conversion of ethane. [b]Reaction rate of ethane converted over various catalysts at 330 and 340 °C. [c]Turnover frequency based on Fe at 330 and 340 °C. [d]Apparent activation energy obtained from Arrhenius plots.

the surface oxygen vacancies. Compared with the area of desorption peaks, it can be found that the amount of oxygen released from Fe_2O_3-S is much higher than those from Fe_2O_3-C and Fe_2O_3-R samples.

3.4. Catalytic Activity. Figure 7A,B reveals that the catalytic activity of prepared materials for ethane destruction follows the sequence of Fe_2O_3-S > Fe_2O_3-C > Fe_2O_3-R. Under a GHSV of 12000 h^{-1}, the Fe_2O_3-S sample can completely decompose 2500 ppm of ethane into CO_2 at 430 °C, which is significantly lower than that of Fe_2O_3-C (500 °C) and Fe_2O_3-R (540 °C). Figure 7C demonstrates that the TOF_{Fe} values of Fe_2O_3-S for ethane oxidation are much higher than those of Fe_2O_3-C and Fe_2O_3-R materials. For example, in Table 4, the calculated TOF_{Fe} values at 330 °C (0.73×10^{-4} h^{-1}) and 340 °C (1.07×10^{-4} h^{-1}) of Fe_2O_3-S are over three (0.22×10^{-4} h^{-1} at 330 °C; 0.30×10^{-4} h^{-1} at 340 °C) and five (0.17×10^{-4} h^{-1} at 330 °C; 0.19×10^{-4} h^{-1} at 340 °C) times higher than those of Fe_2O_3-C and Fe_2O_3-R, respectively, demonstrat-ing the excellent low-temperature activity of Fe_2O_3-S for ethane destruction. In addition to this, further introduction of apparent activation energy (E_a) to compare the catalytic activity of synthetic materials as catalysts and lower E_a value can make ethane more easily oxidized. According to the catalyst map of Arrhenius for ethane oxidation (Figure 7D), the E_a values for ethane oxidation increase in the order Fe_2O_3-S (39.7 kJ mol^{-1}) < Fe_2O_3-C (50.9 kJ mol^{-1}) < Fe_2O_3-R (55.3 kJ mol^{-1}) (Table 4), suggesting that ethane is more easily oxidized over Fe_2O_3-S. Table S4 documented some typical catalysts reported in the literature for ethane oxidation. It is shown that 0.98% Co/1.27% Cu-ZSM-5 had a T_{50} value of 420 °C for ethane combustion,[50] and TiO_2 had a T_{50} value greater °C for ethane combustion.[51] Catalysts ofthan480 $La_{0.7}Sr_{0.3}Mn_{0.75}Co_{0.25}O$ (T_{50} of 476 °C and T_{90} of 485 °C)[52] and $La_{0.7}Bi_{0.3}Mn_{0.75}Co_{0.25}O_3$ (T_{50} of 427 °C and T_{90} of 542 °C)[53] were also less active than the Fe_2O_3-S catalyst. Ethane conversion over the Fe_2O_3-S catalyst was even higher than some noble metal loaded catalysts (e.g., T_{50} and T_{90} of 425 and 475 °C, respectively, over a reported Pt/Al_2O_3 material).[55]

3.5. Catalytic Stability. Reaction stability is a key criterion for industrial applications. Figure 8A shows that Fe_2O_3-S has excellent ethane combustion stability, and only a slight decrease in ethane conversion from 91 to 88% can be observed in the first 30 h. In addition, the stability of Fe_2O_3-S for ethane destruction at a lower temperature of 360 °C was also studied, as displayed in Figure 8B. We found that Fe_2O_3-S possesses satisfied reaction stability at different temperatures,

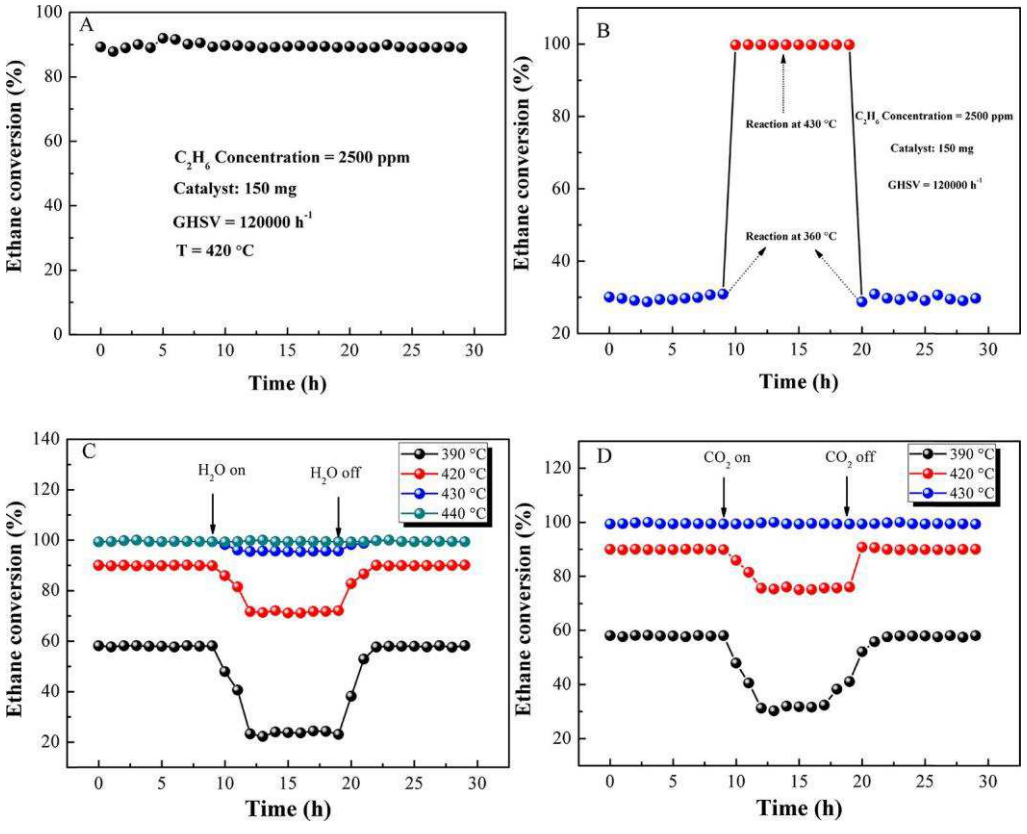

Figure 8. (A, B) Catalytic stability and effect of (C) H_2O and (D) CO_2 on the conversion of ethane over the Fe_2O_3-S catalyst.

and the heating and cooling processes have an insignificant effect on the activity of Fe_2O_3-S. The good stability provides the possibility for the practical elimination of ethane. As shown in Figure S5, the Fe_2O_3-S sample has almost no weight loss in a temperature range of 20−700 °C. The desorption of oxygen and water leading to the weight losses of Fe_2O_3-C (0.2 wt %) and Fe_2O_3-R (0.5 wt %) in a temperature range of 20−100 °C can be attributed to the desorption of H_2O and oxygen,[54] and no weight loss can be found when the temperature is further increased. Above results indicate the good thermal stability of prepared catalysts. Coke deposition on Fe_2O_3-S after the stability test was further analyzed, as shown in Figure S6. The used sample displays two stages of small weight losses in a temperature range of 20−700 °C. The first one at 20−200 °C (0.3 wt %) can be attributed to the combustion/desorption of adsorbed C_2H_6 and the desorption of O_2 and H_2O, and the second one at 200−700 °C (0.9 wt %) corresponds to the combustion of coke deposited on the catalyst,[54] which demonstrates that Fe_2O_3-S is an effective catalyst for catalytic oxidation of C_2H_6. The crystal structure of the Fe_2O_3-S catalyst after reaction was determined by XRD, as shown in Figure S7. The diffraction peaks of the used Fe_2O_3-S sample are almost unchanged compared with the fresh sample, indicating that Fe_2O_3-S has a good chemical stability in catalytic reaction.

The influences of H_2O and CO_2 on catalytic activity of prepared materials for ethane destruction were further investigated. Results show that the addition of H_2O (10 vol %) has negative effects on the conversion of ethane (especially at low temperatures (<420 °C)) due to the competition between water and oxygen adsorption on the catalyst surface; however, this negative effect becomes smaller when the reaction temperature is increased, and the influence of H_2O can be ignored at 440 °C. It is indicated that the deactivation of the catalyst was reversible, and a complete conversion of ethane can be restored when H_2O was no longer added, although recovery took longer at low temperatures.[56] Similarly, the introduction of CO_2 (10 vol %) also has obvious inhibition effects on ethane conversion, and increase in the reaction temperature can obviously reduce this effect (can be ignored at 430 °C). Moreover, when the addition of CO_2 was stopped, the catalytic activity recovered immediately, whereas a longer time was taken to recover the activity of the catalyst after stopping the addition of water vapor, suggesting that H_2O was adsorbed more strongly than CO_2 to active sites.

4. DISCUSSION

4.1. Adsorption of Ethane. Figure S8 shows the in situ DRIFTS spectra of O_2 and C_2H_6 adsorption on prepared samples at room temperature. The IR bands in the region of 3100−2800 cm^{-1} can be assigned to the C−H stretching (ν_{CH}) of alkanes or adsorbed C−H bond containing species, and the peaks at 3000−2850 cm^{-1} can be attributed to the ν_{CH} of C_2H_6.[57] A broad band with a maximum at 3700−3100 cm^{-1} belongs to the sorbed water or acidic OH groups that are hydrogen-bonded to the basic oxygen atoms of the catalysts.[58] It is well known that stretching bands for gaseous ethane were at 2954 and 2994 cm^{-1}.[59] Table S3 reveals that the position of C−H stretching bands for adsorbed ethane over Fe_2O_3-S, Fe_2O_3-C, and Fe_2O_3-R samples is similar, while all the bands are red-shifted to some extent in comparison with those of gaseous ethane due to a combination of ligand-to-metal electron donation from the C−H σ-bond to vacant Fe^{3+} s-orbit combined with the metal-to-ligand back donation from the iron d_π-orbital to C-H σ*-orbit because these interactions lead

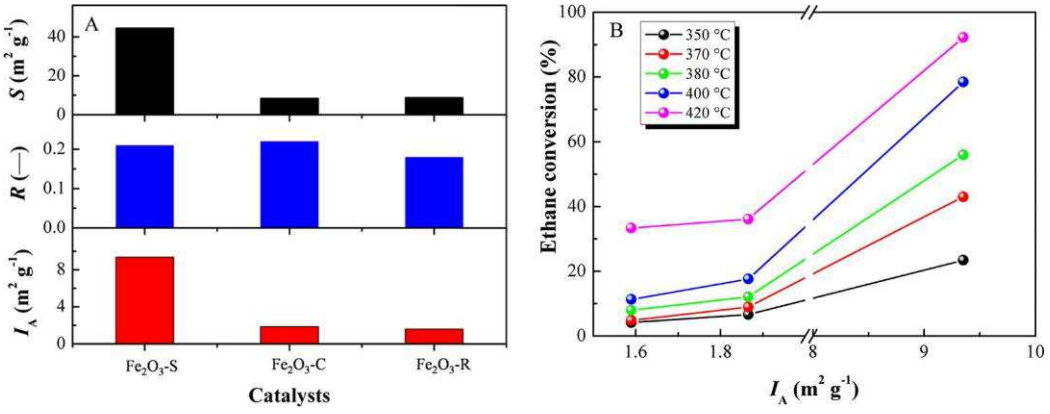

Figure 9. (A) Correlation between S, R, and I_A. (B) Relation between the conversion of ethane and index I_A for all catalysts.

to a very marked weakening of the C−H bond.[59,60] It has been proved that the adsorption of light alkanes by metal oxides in the form of cations results in the change of relative intensity distribution of absorption bands, which largely depends on the properties of cations and metallic oxides.[60] According to the adsorption strength of ethane on all samples, it is found that Fe_2O_3-C is easier to adsorb water than ethane. However, compared with water, it has stronger adsorption for ethane on Fe_2O_3-S and Fe_2O_3-R. It is also shown that the strongest perturbation and polarization oscillations are initially fully symmetrical C−H stretching oscillations, which are directly related to the chemical activation of adsorbed molecules.[61] The greatest red shift of the C−H band was observed for C_2H_6 adsorption on Fe_2O_3-S. This means that Fe_2O_3-S has stronger chemical activation for ethane molecules.[61]

Figure S9 shows the in situ DRIFT spectra of ethane and air adsorption over synthesized catalysts at different temperatures. The intensity of bands at 3700−3100 cm^{-1} shows a continuous reduction (disappeared at 150 °C) when increasing the temperature, indicating the removal of sorbed water from materials.[62] It should be noted that the intensity variation of bands at 3100−2800 cm^{-1} assigned to the C−H stretching (ν_{CH}) of alkanes or adsorbed C−H bond containing species over Fe_2O_3-S (even visible at 200 °C) is much smaller than those over Fe_2O_3-C and Fe_2O_3-R materials, suggesting the strongest ethane adsorption (dissociative adsorption) over the Fe_2O_3-S sample. As shown in Figure S9, for Fe_2O_3-S, the intensity of the bands in the region of 2800−3100 cm^{-1} is the strongest among all samples, indicating that ethane adsorbed on Fe_2O_3-S has a lower activation barrier.[63]

4.2. Correlation of Physicochemical Property and Activity. Specific surface area, concentration and distribution of reactive oxygen species, surface defects and oxygen vacancies, and catalyst reducibility can affect its catalytic performance in oxidation reaction. Zheng et al.[8] proved that the high density of Fe atoms on the exposure {110} planes of α-Fe_2O_3 leads to high activity for catalytic combustion of CO. Kameoka et al.[56] stated that surface Fe sites on $La_{1-x}Sr_xFeO_3$ (x = 0.0−1.0) perovskites are an active species for methane combustion.

Kouotou et al.[1] proved that the more iron content in α-Fe_2O_3 exposed planes, the more active sites for catalytic for catalytic combustion of propene. As it is known, the density of active sites such as the iron atoms is different over various exposed planes in a hematite crystal structure. Table 1 shows that the specific surface area of prepared catalysts and the surface metal compositions obtained from XPS analysis are included in Figure 9. Fe/(Fe + O), defined as the R ratio, is an important factor representing α-F_2O_3 catalyst activity. Surface area plays a role in catalyst activity, the product of the BET surface area (S) and R, defined as the index I_A.[56] It is worth noting that the content of iron atoms over all catalysts is smaller than two-thirds because all catalysts adsorbed a large amount of oxygen on their surface. Figure 9 shows the relationships of different parameters (S, R, and I_A; I_A and ethane conversion) of different catalysts, and results indicate that the surface Fe content over catalysts is directly proportional to the conversion of ethane. F_2O_3-S has a maximum I_A value (9.35 m^2 g^{-1}) and has the highest catalytic activity for catalytic oxidation of ethane.

The Mars van Krevelen (MVK) mechanism has been widely used in interpreting the catalytic oxidation process of hydrocarbons, especially for hydrocarbon oxidation over transition metal oxides, which involves a redox cycle (migration of bulk oxygen to the catalyst surface to oxidize hydrocarbon molecules and replace the bulk oxygen by oxygen from the gas phase) and is closely related to the mobility of the lattice oxygen.[1] As such, the oxygen mobility associated with catalyst reducibility is an important factor for the MVK mechanism.[64] Taking into account the TPR results, it can be concluded that the lattice oxygen mobility in the prepared samples is in the order of F_2O_3-S > F_2O_3-C > F_2O_3-R. High lattice oxygen mobility can accelerate the redox cycle in ethane oxidation and guarantee the superior activity of F_2O_3-S. On the basis of the MVK mechanism and in situ DRIFTS results displayed in Figure S8, a reaction scheme for ethane oxidation was proposed: First, ethane is considered to be adsorbed dissociatively on the surface of the catalyst with extraction of a hydrogen atom and then the release of oxygen atom along with the reduction of the catalyst. Finally, oxygen from the gas phase will reoxidize the reduced iron cations to Fe_2O_3.[65]

XPS results reveal that the percentage of Oβ on the F_2O_3-S catalyst (0.72) is higher than those of F_2O_3-C (0.59) and F_2O_3-R (0.55), indicating that F_2O_3-S possesses higher concentration of chemisorbed oxygen species, which leads to higher proportion of Fe^{3+} in F_2O_3-S and has generated more oxygen vacancies (Figure 9).[66] Results of EELS (Figure 6) and Raman (Figure 4) also suggest that the concentration of oxygen vacancies on F_2O_3-S is higher than those of F_2O_3-C and F_2O_3-R. Above results indicate that the F_2O_3-S sample can produce more reactive oxygen species participating in the oxidation of ethane. Additionally, Mössbauer spectroscopy and Raman

results reveal that there are more defect sites over F_2O_3-S than F_2O_3-C and F_2O_3-R samples, which enhance the oxygen transfer and reduction efficiency, promoting the ethane oxidation rate.[66]

4.3. Formation Energy of Oxygen Vacancy. Oxygen vacancies are suggested to play an important role in the decomposition of ethane, and its activity much rests with the nature of oxygen vacancy.[67] In the present work, the formation energy of a single O defect at α-Fe_2O_3 exposed facets is studied by DFT calculations, as shown in Figure 10. Results

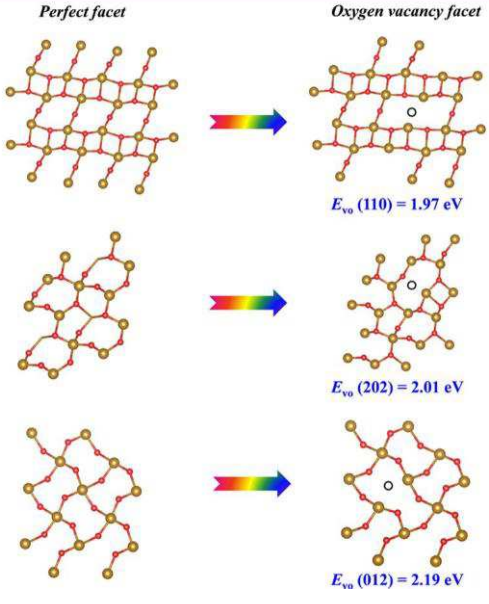

Figure 10. Formation energy of oxygen vacancy over α-Fe_2O_3 with different exposed facets.

demonstrate that the formation energy of oxygen vacancy on the (110) facet (E_{vo} (110) = 1.97 eV) is lower than those of (202) facet (E_{vo} (202) = 2.01 eV) and (012) facet (E_{vo} (012) = 2.19 eV), indicating that the oxygen vacancies are more easier to form on (110) facets of F_2O_3-S (consistent with the in situ Raman results (Figure S2)), endowing the superior ethane destruction activity of the F_2O_3-S catalyst.

4.4. Adsorption of O_2, C_2H_6, and H_2O on Exposed Facets. The O_2 adsorption capability is a very important parameter for VOC oxidation reactions according to the MVK mechanism. As such, the adsorption energy of O_2 on different perfect facets and facets with oxygen vacancies was obtained by DFT (Figure 11). The perfect facets of (110), (202), and (12) have an analogous adsorption capacity for oxygen, and the adsorption energy is very small (0.2 eV); it shows that the adsorption of O_2 on all perfect facets showed very weak physical adsorption. However, when the oxygen vacancy is introduced to the crystal surface, the adsorption energy of molecular O_2 on all facets becomes higher, which indicates that oxygen vacancy is more conducive to catalytic oxidation of ethane. The adsorption energies of O_2 on facets with oxygen vacancies of (110), (202), and (012) are 1.58, 1.55 and 1.22 eV, respectively (Figure 11), indicating that O_2 is easily adsorbed on the face of (110). In addition, the (110) surface is strongly bonded with O_2 with the O−O bond distance, which is 1.405 Å. The longer bond length than this on the (202) (1.394 Å) and (012) (1.371 Å) facets indicates that O_2 can be destroyed more and activated easily. The strong adsorption of O_2 on the (110) surface facilitates the quick addition of oxygen consumed by the oxidation reaction and is beneficial to the catalytic oxidation of ethane. The corresponding adsorption energies of ethane on (110), (202), and (012) surfaces were calculated to be −0.26, −0.23, and −0.21 eV, respectively (Figure S10), in good accordance to the order of catalytic performance of prepared materials. In addition, the adsorption energy of water on the (110) surface is calculated. As shown in Figure S11, we found that the adsorption energy of H_2O (−1.54 eV) is close to that of O_2 (−1.58 eV), suggesting the reason for the competition between water and oxygen adsorption on the surface of the catalyst.

Figure 12 shows the total electronic density of states (DOS) and its projections over the 3d orbitals of iron cations and the 2p orbitals of the O anions for (110), (202), and (012)

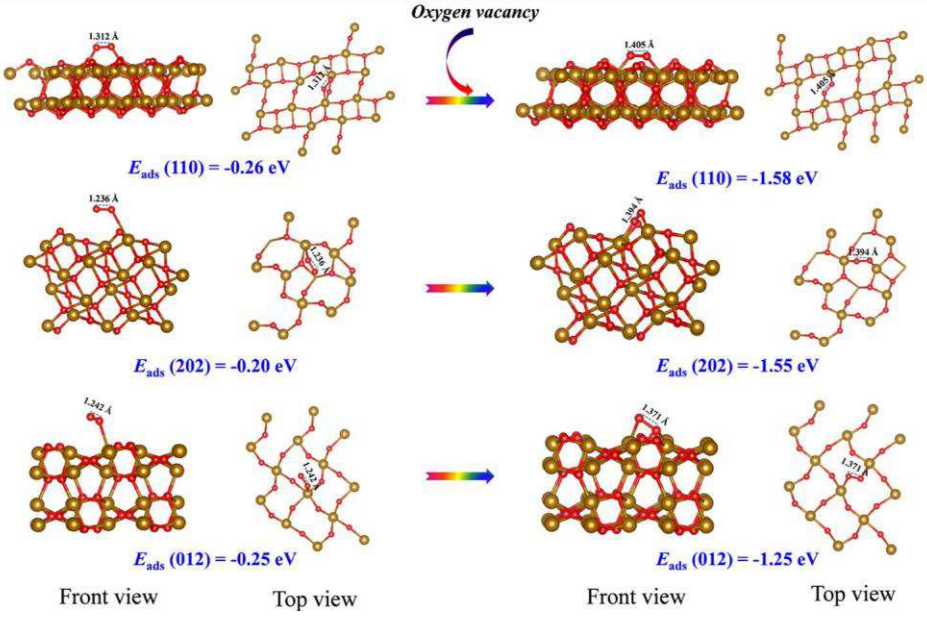

Figure 11. Adsorption energy of O_2 over α-Fe_2O_3 with different exposed perfect crystal surfaces and crystal surfaces with oxygen vacancies.

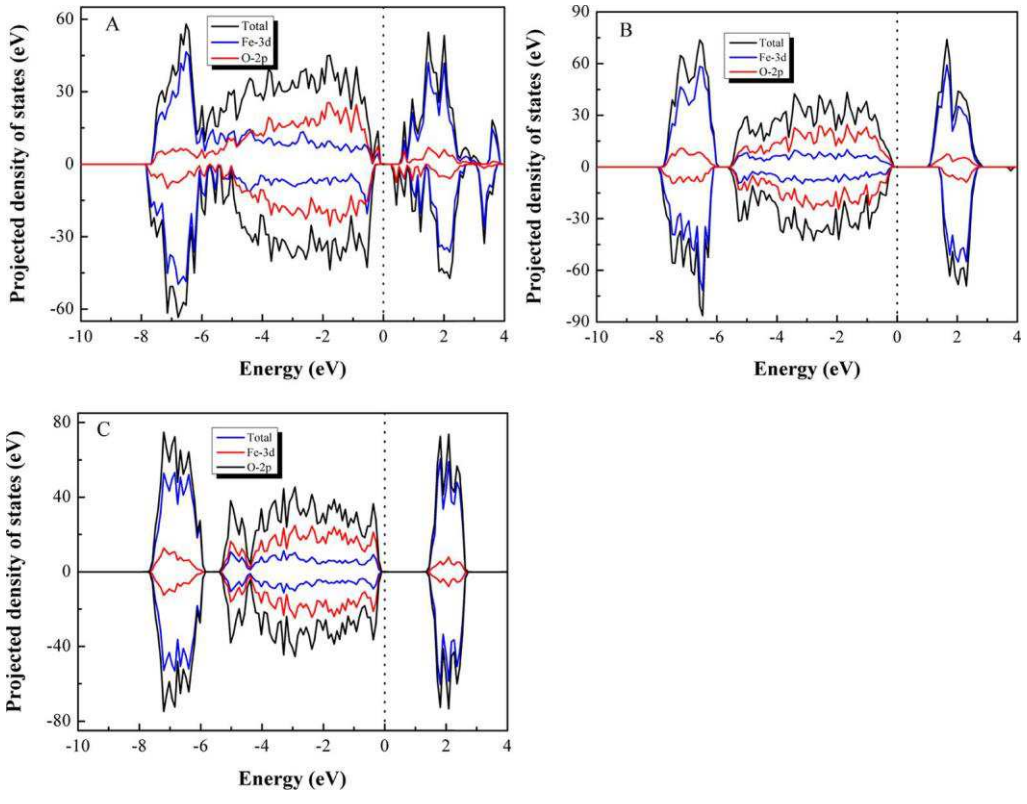

Figure 12. Projected density of states (PDOS) of different catalysts: (A) Fe_2O_3-S, (B) Fe_2O_3-C, and (C) Fe_2O_3-R (Fe 3d and O 2p states are plotted as solid and dotted lines, respectively). The Fermi energy is set to be 0, highlighted by a black vertical dashed line.

surfaces of α-Fe_2O_3.[68] For all samples, the top of the valence band is mainly of O 2p character, while the occupied 3d levels of Fe lie around 6−8 eV below the Fermi level. The unoccupied 3d levels of Fe, which have an octahedral coordination, mainly populate the bottom of the conduction band.[68] As such, maghemite is a charge transfer-type insulator, and the first excitation term should correspond to the transfer of electrons from O^{2-} anions to octahedral Fe^{3+} cations.[68] Furthermore, the existence of some of these surface states in the bulk band gap indicates the variation of metal character-istics in all of these models.[68] By gathering the DOSs of surface ions, the (110) surface shows the highest metallic behavior with a narrow band gap of 0.26 eV compared to the (202) and
(12) surfaces with band gaps of about 1.11 and 1.46 eV, respectively. These results highlight the promising role of the
(110) surface of α-Fe_2O_3 in surface redox reactions.

For the (110) surface, the electronic state covers most of the bulk band gap regions and shows higher polarity on the surface than other regions because the stabilization of the polarized surface can be achieved by the depolarization field, which causes some changes in the electronic surface state so that some states appear in the bulk band gap region.[68] Subsequently, neutralization of the polarized surfaces can be obtained by the flow of free charge within the surface layer.[68] The (110) surface shows the highest metal features with a very narrow band gap. Furthermore, these states can provide a depolarizing field, which has a vital role in the stabilization of the polar termination.[68]

Finally, the (100) surfaces are more polar than stoichiom-etry, which cause a relatively low stability of these models. It is indicted that the (110) surface is more likely to lose electrons, which makes it easier for oxidation−reduction reactions.

5. CONCLUSIONS

In summary, α-Fe_2O_3 samples with different morphologies were successfully synthesized by the simple solvothermal method. Fe_2O_3-S exhibits superior catalytic activity in the oxidation of ethane due to its highest low-temperature reducibility and largest number of active surface lattice defects and oxygen vacancies. Theoretical calculations confirm that the exposed (110) facet has the lowest oxygen vacancy formation energy (1.97 eV), which is favorable for the formation of surface active oxygen species. In addition, the exposed (110) facets facilitate the adsorption and activation of O_2 (E_{ads} = −1.58 eV; bond length of adsorbed O_2 is 1.405 Å, which is far greater than the distances of 1.394 and 1.371 Å for (202) and
(12) facets) and an easier redox process, which promotes the ethane oxidation activity. These results can provide a simple and effective strategy for the engineering design of reaction exposed surfaces and deepen the understanding of the small side-related catalytic activity of α-Fe_2O_3 in hydrocarbon destruction.

ASSOCIATED CONTENT

N_2 adsorption−desorption isotherms and pore size distribution, intensity of the fitted E_g, LO, and T bands present in the Raman spectra, in situ Raman spectra, TPR profiles, in situ DRIFTS spectra of ethane adsorption, summary of some active catalysts for ethane oxidation, and adsorption energy of ethane and H_2O on catalysts (PDF)

AUTHOR INFORMATION

Corresponding Author

*E-mail: chi_he@xjtu.edu.cn. Tel.: +86 29 82663857. Fax: +86 29 82663857.

ORCID

Yanke Yu: 0000-0003-4214-8284

Chi He: 0000-0001-6403-1277

Author Contributions

°Y.J. and T.Y. contributed equally to this work.

Notes

The authors declare no competing financial interest.

ACKNOWLEDGMENTS

This work was financially supported by the National Natural Science Foundation of China (21677114, 21876139, and 21477095), the National Key Research and Development Program (2016YFC0204201), and the Fundamental Research Funds for the Central Universities (xjj2017170). The valuable comments from the editor and anonymous reviewers are much appreciated.

REFERENCES

(1) Kouotou, P. M.; Tian, Z.-Y.; Vieker, H.; Beyer, A.; Gölzhauser, A.; Kohse-Höinghaus, K. Selective Synthesis of α-Fe_2O_3 thin Films and Effect of the Deposition Temperature and Lattice Oxygen on the Catalytic Combustion of Propene. J. Mater. Chem. A 2013, 1, 10495− 10504.

(2) Alifanti, M.; Bueno, G.; Parvulescu, V.; Parvulescu, V. I.; Cortés Corberán, V. Oxidation of Ethane on High Specific Surface $SmCoO_3$ and $PrCoO_3$ Perovskites. Catal. Today 2009, 143, 309−314.

(3) Suarez-Vazquez, S. I.; Gil, S.; García-Vargas, J. M.; Cruz-Lopez, A.; Giroir-Fendler, A. Catalytic Oxidation of Toluene by $SrTi1-xBxO_3$ (B = Cu and Mn) With Dendritic Morphology Synthesized by One Pot hydrothermal Route. Appl. Catal., B 2018, 223, 201−208.

(4) He, C.; Jiang, Z.; Ma, M.; Zhang, X.; Douthwaite, M.; Shi, J.-W.; Hao, Z. Understanding the Promotional Effect of Mn_2O_3 on Micro−/ Mesoporous Hybrid Silica Nanocubic-Supported Pt Catalysts for the Low-Temperature Destruction of Methyl Ethyl Ketone: An Experimental and Theoretical Study. ACS Catal. 2018, 8, 4213−4229.

(5) Liu, J.; Meeprasert, J.; Namuangruk, S.; Zha, K.; Li, H.; Huang, L.; Maitarad, P.; Shi, L.; Zhang, D. Facet−Activity Relationship of TiO_2 in Fe_2O_3/TiO_2 Nanocatalysts for Selective Catalytic Reduction of NO with NH_3: In Situ DRIFTs and DFT Studies. J. Phys. Chem. C 2017, 121, 4970−4979.

(6) He, C.; Cheng, J.; Zhang, X.; Douthwaite, M.; Pattison, S.; Hao, Z. Recent Advances in the Catalytic Oxidation of Volatile Organic Compounds: A Review Based on Pollutant Sorts and Sources. Chem. Rev. 2019, DOI: 10.1021/acs.chemrev.8b00408.

(7) Hu, X.; Huang, L.; Zhang, J.; Li, H.; Zha, K.; Shi, L.; Zhang, D. Facile and Template-free Fabrication of Mesoporous 3D Nanosphere-like $Mn_xCo_{3-x}O_4$ as Highly Effective Catalysts for Low Temperature SCR of NO_x with NH_3. J. Mater. Chem. A 2018, 6, 2952−2963.

(8) Zheng, Y. H.; Cheng, Y.; Wang, Y. S.; Bao, F.; Zhou, L. H.; Wei, X. F.; Zhang, Y. Y.; Zheng, Q. Quasicubic alpha-Fe2O3 Nanoparticles with Excellent Catalytic Performance. J. Phys. Chem. B 2006, 110, 3093−3097.

(9) Jian, Y.; Ma, M.; Chen, C.; Liu, C.; Yu, Y.; Hao, Z.; He, C. Tuning the Micromorphology and Exposed Facets of MnO_x Promotes Methyl Ethyl Ketone Low-temperature Abatement: Boosting Oxygen Activation and Electron Transmission. Catal. Sci. Technol. 2018, 8, 3863−3875.

(10) Rong, S.; Zhang, P.; Liu, F.; Yang, Y. Engineering Crystal Facet of α-MnO_2 Nanowire for Highly Efficient Catalytic Oxidation of Carcinogenic Airborne Formaldehyde. ACS Catal. 2018, 8, 3435− 3446.

(11) Yao, W.-T.; Yu, S.-H.; Wu, Q.-S. From Mesostructured Wurtzite ZnS-nanowire/amine Nanocomposites to ZnS Nanowires Exhibiting Quantum Size Effects: A Mild-solution Chemistry Approach. Adv. Funct. Mater. 2007, 17, 623−631.

(12) Wang, C.; Hou, Y.; Kim, J.; Sun, S. A General Strategy for Synthesizing FePt Nanowires and Nanorods. Angew. Chem., Int. Ed. 2007, 46, 6333−6335.

(13) Bachmann, J.; Jing, J.; Knez, M.; Barth, S.; Shen, H.; Mathur, S.; Gosele, U.; Nielsch, K. Ordered Iron Oxide Nanotube Arrays of Controlled Geometry and Tunable Magnetism by Atomic Layer Deposition. J. Am. Chem. Soc. 2007, 129, 9554−9555.

(14) Zhang, L.; Ruh, E.; Grützmacher, D.; Dong, L.; Bell, D. J.; Nelson, B. J.; Schonenberger, C. Anomalous Coiling of SiGe/Si and SiGe/Si/Cr Helical Nanobelts. Nano Lett. 2006, 6, 1311−1317.

(15) Xu, L. Q.; Zhan, J. H.; Hu, J. Q.; Bando, Y.; Yuan, X. L.; Sekiguchi, T.; Mitome, M.; Golberg, D. High-yield Synthesis of Rhombohedral Boron Nitride Triangular Nanoplates. Adv. Mater. 2007, 19, 2141−2144.

(16) Paek, J.; Lee, C. H.; Choi, J.; Choi, S.-Y.; Kim, A.; Lee, J. W.; Lee, K. Gadolinium Oxide Nanoring and Nanoplate: Anisotropic Shape Control. Cryst. Growth Des. 2007, 7, 1378−1380.

(17) Zhou, K.; Wang, X.; Sun, X.; Peng, Q.; Li, Y. Enhanced Catalytic Activity of Ceria Nanorods from Well-defined Reactive Crystal Planes. J. Catal. 2005, 229, 206−212.

(18) Chen, A.; Zhou, Y.; Ta, N.; Li, Y.; Shen, W. Redox Properties and Catalytic Performance of Ceria-zirconia Nanorods. Catal. Sci. Technol. 2015, 5, 4184−4192.

(19) Xie, Y.; Yu, Y.; Gong, X.; Guo, Y.; Guo, Y.; Wang, Y.; Lu, G. Effect of the Crystal Plane Figure on the Catalytic Performance of MnO_2 for the Total Oxidation of Propane. CrystEngComm 2015, 17, 3005−3014.

(20) Qiu, G.; Huang, H.; Genuino, H.; Opembe, N.; Stafford, L.; Dharmarathna, S.; Suib, S. L. Microwave-Assisted Hydrothermal Synthesis of Nanosized α-Fe_2O_3 for Catalysts and Adsorbents. J. Phys. Chem. C 2011, 115, 19626−19631.

(21) Yoo, S.-G.; Kim, J.-H.; Kim, U.-H.; Jung, J.-S.; Lee, S.-H. Comparison of the Kinetic Behaviors of Fe_2O_3 Spherical Submicron Clusters and Fe_2O_3 Fine Powder Catalysts for CO Oxidation. Bull. Korean Chem. Soc. 2014, 35, 1379−1384.

(22) Wu, J.; Su, T.; Jiang, Y.; Xie, X.; Qin, Z.; Ji, H. In situ DRIFTS Study of O_3 Adsorption on CaO, γ-Al_2O_3 , CuO, α-Fe_2O_3 and ZnO at Room Temperature for the Catalytic Ozonation of Cinnamaldehyde. Appl. Surf. Sci. 2017, 412, 290−305.

(23) Ramezani, Z.; Shekarriz, M.; Behfar, A. A.; Kiamarzi, S. Pre-Concentration and Separation of Perphenazine Using Picric Acid Loaded α-Fe_2O_3 Nanoparticles: HPLC Syringe Filter as the Particles Support. J. Braz. Chem. Soc. 2017, 28, 2172−2179.

(24) Larcher, D.; Sudant, G.; Patrice, R.; Tarascon, J. M. Some Insights on the Use of Polyols-based Metal Alkoxides Powders as Precursors for Tailored Metal-oxides Particles. Chem. Mater. 2003, 15, 3543−3551.

(25) Fang, J.; Xu, J.; Chen, J.; Huang, X.; Wang, X. Enhanced Photocatalytic Activity of Molecular Imprinted Nano α-Fe_2O_3 by Hydrothermal Synthesis Using Methylene Blue as Structure-directing Agent. Colloids Surf., A 2016, 508, 124−134.

(26) Liu, A.; Xia, Z.; Zhou, W.; Huang, S. Well-dispersed Hematite Nanoparticles Decorating Graphene Nanosheets: Characterization and Performance for Methyl Orange Removal. J. Environ. Chem. Eng. 2017, 5, 6039−6044.

(27) Wang, J.; Wang, C.; Tong, S. A novel composite Fe-N/O Catalyst for the Effective Enhancement of Oxidative Capacity of Persulfate at Ambient Temperature. Catal. Commun. 2018, 103, 105− 109.

(28) Xie, P.; Ma, Z.; Meng, T.; Huang, C.; Miao, C.; Yue, Y.; Hua, W.; Gao, Z. Active Fe Species of Fe_2O_3/Fe-Silicalite-1 Nanowires in N_2O Decomposition. J. Mol. Catal. A: Chem. 2015, 409, 50−58.

(29) Tirupanyam, B. V.; Srinivas, C.; Meena, S. S.; Yusuf, S. M.; Satish Kumar, A.; Sastry, D. L.; Seshubai, V. Investigation of Structural and Magnetic Properties of Co-precipitated Mn−Ni Ferrite

Nanoparticles in the Presence of α-Fe_2O_3 Phase. J. Magn. Magn. Mater. 2015, 392, 101−106.
(30) Nag, S.; Roychowdhury, A.; Ds, D.; Mukherjee, S. Synthesis of α-Fe_2O_3-functionalised Graphene Oxide Nanocomposite by a Facile Low Temperature Method and Study of its Magnetic and Hyperfine Properties. Mater. Res. Bull. 2016, 74, 109−116.
(31) Idczak, R.; Konieczny, R.; Chojcan, J. Study of defects in Fe−Re and Fe−Mo Alloys by the Mössbauer and Positron Annihilation Spectroscopies. Solid State Commun. 2012, 152, 1924−1928.
(32) Cheng, X.; Li, K.; Wei, Y.; Zhu, X.; Tian, D. Modification of KNO_3 on the reducibility and reactivity of Fe_2O_3-based oxygen carriers for chemical-looping combustion of methane. Can. J. Chem. Eng. 2017, 95, 1569−1578.
(33) Almeida, T. P.; Fay, M. W.; Zhu, Y.; Brown, P. D. Hydrothermal Growth Mechanism of α-Fe_2O_3 Nanorods Derived by Near in Situ Analysis. Nanoscale 2010, 2, 2390−2399.
(34) Guo, Y.; Zhang, S.; Zhu, J.; Su, L.; Xie, X.; Li, Z. Effects of Pt on Physicochemical Properties over Pd Based Catalysts for Methanol Total Oxidation. Appl. Surf. Sci. 2017, 416, 358−364.
(35) Zhou, H.; Li, K.; Zhao, B.; Deng, W.; Su, Y.; Zhong, F. Surface Properties and Reactivity of Fe/Al_2O_3/cordierite Catalysts for NO Reduction by C_2H_6: Effects of calcination temperature. Chem. Eng. J. 2017, 326, 737−744.
(36) Cardillo, D.; Tehei, M.; Hossain, S.; Islam, M.; Bogusz, K.; Shi, D.; Mitchell, D.; Lerch, M.; Rosenfeld, A.; Corde, S.; Konstantinov, K. Synthesis-Dependent Surface Defects and Morphology of Hematite Nanoparticles and Their Effect on Cytotoxicity in Vitro. ACS Appl. Mater. Interfaces 2016, 8, 5867−5876.
(37) Grosvenor, A. P.; Kobe, B. A.; Biesinger, M. C.; McIntyre, N. S. Investigation of Multiplet Splitting of Fe 2p XPS Spectra and Bonding in Iron Compounds. Surf. Interface Anal. 2004, 36, 1564−1574.
(38) Chernyshova, I. V.; Hochella, M. F., Jr.; Madden, A. S. Size-Dependent Structural Transformations of Hematite Nanoparticles. 1.Phase Transition. Phys. Chem. Chem. Phys. 2007, 9, 1736−1750.
(39) Łojewska, J.; Knapik, A.; Kołodziej, A.; Jodłowski, P. Far Field Combined AFM and Micro-Raman Imaging for Characterisation of Surface of Structured Catalysts: Example of Pd Doped CoO_x Catalysts on Precalcined Kanthal Steel. Top. Catal. 2013, 56, 1088−1095.
(40) Chen, J.; Chen, X.; Xu, W.; Xu, Z.; Chen, J.; Jia, H.; Chen, J. Hydrolysis Driving Redox Reaction to Synthesize Mn-Fe Binary Oxides as Highly Active Catalysts for the Removal of Toluene. Chem. Eng. J. 2017, 330, 281−293.
(41) Lin, X.; Li, S.; He, H.; Wu, Z.; Wu, J.; Chen, L.; Ye, D.; Fu, M. Evolution of Oxygen Vacancies in MnO_x-CeO_2 Mixed Oxides for Soot Oxidation. Appl. Catal., B 2018, 223, 91−102.
(42) Tsoncheva, T.; Ivanova, R.; Dimitrov, M.; Paneva, D.; Kovacheva, D.; Henych, J.; Vomacka, P.; Kormunda, M.; Velinov, N.; Mitov, I.; Stengl, V. Template-assisted Hydrothermally Synthesized Iron-titanium Binary Oxides and their Application as Catalysts for Ethyl Acetate Oxidation. Appl. Catal., A 2016, 528, 24−35.
(43) Chueh, Y.-L.; Lai, M.-W.; Liang, J.-Q.; Chou, L.-J.; Wang, Z.-L. Systematic Study of the Growth of Aligned Arrays of α-Fe_2O_3 and Fe_3O_4 Nanowires by a Vapor−Solid Process. Adv. Funct. Mater. 2006, 16, 2243−2251.
(44) Colliex, C.; Manoubi, T.; Ortiz, C. Electron-energy-loss-spectroscopy Near-edge Fine structures in the Iron-oxygen System. Phys. Rev. B 1991, 44, 11402−11411.
(45) Alshehri, A. A.; Narasimharao, K. Low Temperature Oxidation of Carbon Monoxide over Mesoporous Au-Fe_2O_3 Catalysts. J. Nanomater. 2017, 2017, 1−14.
(46) Wang, F.; Dai, H.; Deng, J.; Bai, G.; Ji, K.; Liu, Y. Manganese Oxides With Rod-, Wire-, Tube-, and Flower-like Morphologies: Highly Effective Catalysts for the Removal of Toluene. Environ. Sci. Technol. 2012, 46, 4034−4041.
(47) Wang, Z.; Wang, W.; Zhang, L.; Jiang, D. Surface Oxygen Vacancies on Co_3O_4 Mediated Catalytic Formaldehyde Oxidation at Room Temperature. Catal. Sci. Technol. 2016, 6, 3845−3853.
(48) Liu, Q.; Wang, L.-C.; Chen, M.; Cao, Y.; He, H.-Y.; Fan, K.-N. Dry Citrate-precursor Synthesized Nanocrystalline Cobalt Oxide as Highly Active Catalyst for Total Oxidation of Propane. J. Catal. 2009, 263, 104−113.
(49) Kucherov, A. V.; Hubbard, C. P.; Kucherova, T. N.; Shelef, M. Stabilization of the Ethane Oxidation Catalytic Activity of Cu-ZSM-5. Appl. Catal., B 1996, 7, 285−298.
(50) Tahir, S. F.; Koh, C. A. Catalytic Oxidation for Air Pollution Control. Environ. Sci. Pollut. Res. 1996, 3, 20−23.
(51) Gholizadeh, A.; Malekzadeh, A.; Ghiasi, M. Structural and Magnetic Features of $La_{0.7}Sr_{0.3}Mn_{1-x}Co_xO_3$ Nano-catalysts for Ethane Combustion and CO Oxidation. Ceram. Int. 2016, 42, 5707−5717.
(52) Gholizadeh, A.; Malekzadeh, A. Structural and Redox Features of $La_{0.7}Bi_{0.3}Mn_{1-x}Co_xO_3$ Nanoperovskites for Ethane Combustion and CO Oxidation. Int. J. Appl. Ceram. Technol. 2017, 14, 404−412.
(53) Dadi, R. K.; Luss, D.; Balakotaiah, V. Dynamic Hysteresis in Monolith Reactors and Hysteresis Effects During Co-oxidation of CO andC_2H_6. Chem. Eng. J. 2016, 297, 325−340.
(54) Fareghi-Alamdari, R.; Niri, M. N.; Hazarkhani, H.; Zekri, N. Diacidic ionic Liquid Supported on Magnetic-silica Nanocomposite: a Novel, Stable, and Reusable Catalyst for Selective Diester Production. J. Iran. Chem. Soc. 2018, 15, 2615−2629.
(55) Wang, C.-H.; Chen, C.-L.; Weng, H.-S. Surface Properties and Catalytic Performance of $La_{1-x}Sr_xFeO_3$ Perovskite-type Oxides for Methane Combustion. Chemosphere 2004, 57, 1131−1138.
(56) Kameoka, S.; Kita, K.; Tanaka, S.-i.; Nobukawa, T.; Ito, S.-i.; Tomishige, K.; Miyadera, T.; Kunimori, K. Enhancement of C_2H_6 Oxidation by O_2 in the Presence of N_2O Over Fe ion-exchanged BEA Zeolite Catalyst. Catal. Lett. 2002, 79, 63−67.
(57) Kazansky, V. B.; Pidko, E. A. Intensities of IR Stretching Bands as a Criterion of Polarization and Initial Chemical Activation of Adsorbed Molecules in Acid Catalysis. Ethane Adsorption and Dehydrogenation by Zinc ions in ZnZSM-5 Zeolite. J. Phys. Chem. B 2005, 109, 2103−2108.
(58) Kazansky, V. B.; Subbotina, I. R.; Jentoft, F. C.; Schlogl, R. Intensities of C−H IR Stretching Bands of Ethane and Propane Adsorbed by Zeolites as a New Spectral Criterion of their Chemical Activation via Polarization Resulting from Stretching of Chemical Bonds. J. Phys. Chem. B 2006, 110, 17468−17477.
(59) Pidko, E.; Kazansky, V. σ-Type Ethane Adsorption Complexes with Cu^+ ions in Cu(i)-ZSM-5 Zeolite. Combined DRIFTS and DFT Study. Phys. Chem. Chem. Phys. 2005, 7, 1939−1944.
(60) Shilina, M. I.; Vasilevskii, G. Y.; Rostovshchikova, T. N.; Murzin, V. Y. Unusual Coordination State of Cobalt ions in Zeolites Modified by Aluminum Chloride. Dalton Trans. 2015, 44, 13282− 13293.
(61) Pirayavaraporn, C.; Rades, T.; Gordon, K. C.; Tucker, I. G. Quantification of the Types of Water in Eudragit RLPO Polymer and the Kinetics of Water Loss using FTIR. Int. J. Pharm. 2013, 458, 90− 98.
(62) Kazansky, V. B.; Subbotina, I. R.; Pronin, A. A.; Schlogl, R.; Jentoft, F. C. Unusual infrared spectrum of ethane adsorbed by gallium oxide. J. Phys. Chem. B 2006, 110, 7975−7978.
(63) Pan, H.; Jian, Y.; Chen, C.; He, C.; Hao, Z.; Shen, Z.; Liu, H. Sphere-Shaped Mn_3O_4 Catalyst with Remarkable Low-Temperature Activity for Methyl-Ethyl-Ketone Combustion. Environ. Sci. Technol. 2017, 51, 6288−6297.
(64) Karamullaoglu, G.; Dogu, T. Oxidative Dehydrogenation of Ethane Over a Monolith Coated by Molybdenum-vanadium-niobium Mixed-oxide Catalyst. Chem. Eng. Commun. 2003, 190, 1427−1438.
(65) Tan, H.; Wang, J.; Yu, S.; Zhou, K. Support Morphology-Dependent Catalytic Activity of Pd/CeO_2 for Formaldehyde Oxidation. Environ. Sci. Technol. 2015, 49, 8675−8682.
(66) Zhu, L.; Wang, J.; Rong, S.; Wang, H.; Zhang, P. Cerium Modified Birnessite-type MnO_2 for Gaseous Formaldehyde Oxidation at Low Temperature. Appl. Catal., B 2017, 211, 212−221.
(67) Grau-Crespo, R.; Al-Baitai, A. Y.; Saadoune, I.; De Leeuw, N. H. Vacancy Ordering and Electronic Sructure of gamma-Fe_2O_3 (maghemite): a Theoretical Investigation. J. Phys.: Condens. Matter 2010, 22, 255401.

(68) Hashim, A. H.; Zayed, A. O. H.; Zain, S. M.; Lee, V. S.; Said, S. M. Electronic, Magnetic and Structural Properties of Co_3O_4 (100) Surface: a DFT+U Study. Appl. Surf. Sci. 2018, 427, 1090−1095.